This is a repository copy of *Torque Generation Mechanism and Performance Evaluation of a Dual-Sided PM Machine with Stator U-Shaped Magnets*.

White Rose Research Online URL for this paper:
https://eprints.whiterose.ac.uk/192667/

Version: Accepted Version

Torque Generation Mechanism and Performance Evaluation of a Dual-Sided PM Machine with Stator U-Shaped Magnets

Ya Li[1], Hui Yang[1]*, *Member*, *IEEE*, Heyun Lin[1], *Senior Member*, *IEEE*, Wei Liu[1], Xing Zhao[2], *Member*, *IEEE*

[1]School of Electrical Engineering, Southeast University, Nanjing, China
[2]Department of Electrical Engineering, The Hong Kong Polytechnic University, Hong Kong, China

Abstract—**This paper proposes a new dual-sided permanent magnet (DSPM) machine with flux-concentrated U-shaped permanent magnets (PMs) in stator, and consequent-pole PMs in rotor, respectively. The proposed DSPM machine can perform a bidirectional field modulation effect (BFME) to enhance the effective harmonics, and hence improving torque capability. A magneto-motive force (MMF)-permeance based model is employed to reveal the torque production mechanism. The torque contributions of main-order working field harmonics are identified and quantified by employing a hybrid finite element (FE)/analytical method with a unified average torque equation. In order to confirm the merits of the proposed design, the basic electromagnetic characteristics of the proposed DSPM configuration are investigated and compared with those of an existing DSPM machine with stator consequent-pole PM design. Besides, in order to further reduce the cogging torque, a parallel complementary (PC) design is adopted for the final prototyping. Finally, a 6-slot/14-pole-pair prototype is manufactured, and some experimental measurements are carried out to validate the theoretical and FE analyses.**

Index Terms—**Bidirectional field modulation effect (BFME), consequent-pole permanent magnet (PM), dual-sided PM machine, torque production mechanism, U-shaped magnet.**

I. INTRODUCTION

DUE to the inherit merits of high torque/power density and high efficiency, permanent magnet (PM) machine is extensively regarded as a candidate for electric vehicles, wind power generation and various industrial application[1]-[2]. Compared with conventional PM machines with magnets mounted on the rotor [3], stator PM machines [4] have a salient rotor structure, armature windings and PMs in their stator side, leading to the advantages of high rotor robustness, good thermal management and easy manufacturing. However, because dominant stationary air-gap field harmonics are absent for the effective torque generation, the stator PM machines normally suffer from compromised torque density than conventional PM machines.

In order to combine the merits of rotor and stator PM machine configurations to enhance the torque capability, a dual-sided PM (DSPM) concept is first introduced by A. Ishizaki [5]. Because PMs are located in both stator and rotor sides, a bidirectional field modulation effect (BFME) can be achieved in DSPM machines [6]-[7]. This implies that DSPM structures can produce multiple air-gap field harmonics, and hence exhibiting higher torque capability than those rotor and stator PM counterparts [6]-[7]. Then, various DSPM machine topologies in term of hybrid excited [8]-[9], linear [10]-[11], dual-stator [12], outer rotor [13]-[14], and memory machine [15]-[16] configurations are newly developed and investigated in recent years.

In addition, four DSPM machines are comparatively studied in [17], which demonstrates that the stator tooth-PM structure has the highest torque density than other counterparts. For enhancing stator tooth-PM flux strengthening effect, two tangentially magnetized PMs with opposite directions are set to each stator tooth-PM [18]. However, the stator tooth-PM machine has the unipolar coil flux linkage, which results in significant magnetic saturation in stator teeth, and hence compromising the torque capability. Besides, the DSPM machines with different stator slot PM configurations are investigated in [19]-[20], which shows that high power factor and high efficiency can be simultaneously achieved. Moreover, the DSPM machines with stator closed-slot configurations are proposed in [21]-[22], which increases the design freedom of stator PM. As a result, the proposed structure exhibits higher torque capability than its existing counterparts [22]. However, the larger flux leakage reduces the PM utilization ratio, and hence results in localized iron saturation in these cases. For enhancing torque capability, some DSPM machines with bipolar stator PM flux structures are proposed [23]-[27]. In order to reduce the flux leakage, a DSPM machine with stator consequent-pole PM is proposed in [23], which shows high torque capability, power factor and flux-weakening capability and efficiency compared with its single-side PM cases. Besides, a non-uniformly distributed stator PM and flux modulation pole design is presented to enhance the main-order working harmonic components for torque production, which exhibits higher torque capability than the uniformly distributed structure [24]. The DSPM machines with complementary stator structures are comparatively studied in [25], which shows that the machine with Fe-N-Fe-N-Fe arrangement exhibits higher torque and PM utilization ratio. In addition, a DSPM machine with stator spoke-type magnets is investigated in [26], which demonstrates that the machine with 14-pole-pair has the highest torque density. Besides, compared with the conventional

consequent pole magnet design [27], a DSPM machine with stator spoke-type magnets configuration exhibits higher torque capability due to its better flux concentrated effect.

This paper aims to provide an insightful understanding of torque generation mechanism and performance evaluation of a novel DSPM machine with stator U-shaped magnets. In Section II, the machine topology is illustrated. In Section III, a hybrid finite element (FE)/analytical method is proposed to quantify the torque contributions of multiple air-gap field working harmonics with the help of a unified average torque equation. In Section IV, in order to confirm the proposed design, a conventional DSPM machine with stator consequent-pole PM design is selected to present a performance comparison. In Section V, a parallel complementary (PC) design is employed in an optimally selected 6-slot/14-pole-pair DSPM structure to reduce the cogging torque. Besides, some experimental measurements are carried out on a 6-slot/14-pole-pair machine prototype in order to confirm the theoretical and FE analyses. Finally, some conclusions are drawn in Section VI.

II. MACHINE TOPOLOGIES

The topology of a 6-slot/14-pole-pair DSPM machine is illustrated in Fig. 1. It can be seen that the machine has consequent-pole PMs in rotor and U-shaped PMs in stator, which enables a BFME for the torque improvement. Besides, the stator U-shaped PM arrangement exhibits high flux concentrated effect, which means that the larger effective working harmonics can be obtained. In addition, it should be noted that some iron bridges are adopted in the stator to strengthen the stator mechanical stability. The main design parameters are tabulated in Table I.
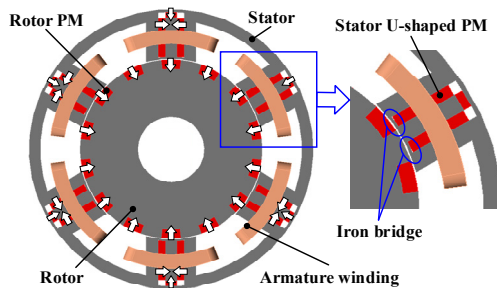

Fig. 1. Topology of 6-slot/14-pole-pair DSPM machine.

TABLE I
MAIN DESIGN PARAMETERS OF THE PROPOSED DSPM MACHINE

Items	DSPM machine
Stator slot number, Z_s	6
Rotor PM pole-pair, Z_r	14
Stator outer diameter, mm	102
Stator yoke thickness, mm	4
Stator PM thickness, mm	2.7
Stator inner diameter, mm	66.2
Air-gap length, mm	0.5
Rotor outer diameter, mm	65.2
Rotor PM thickness, mm	3.4
Rotor PM pole-arc ratio,	0.49
Steel grade	35CS250
PM grade	N42SH
Turns per phase	136
Rated current, A	8

III. TORQUE PRODUCTION MECHANISM

A. PM MMF-Permeance Based Modeling

A simple PM MMF-permeance method is employed to illustrate the torque generation mechanism of the studied DSPM machine. The ideal stator PM MMF distribution can be expressed as

$$F_{SPM} = \sum_{i=0} F_{SPMi} \sin(iZ_s\theta) \qquad (1)$$

where Z_s is the numbers of stator PM pole pairs, F_{SPMi} is the ith stator PM MMF Fourier coefficient. The rotor PM MMF distribution can be expressed as

$$F_{RPM} = \sum_{j=0} F_{RPMj} \sin\left[jZ_r(\theta - \theta_0 - \Omega_r t)\right] \qquad (2)$$

where Z_r is the number of rotor PM pole pairs, θ_0 is the initial rotor position relative to the stator, and Ω_r is the rotor angular speed.

For a doubly salient configurations, the stator and rotor slotting effects can be taken into account respectively. Thus, the air-gap permeance can be synthesized by calculating the stator and rotor permeances, respectively. The air-gap permeance function can be expressed as [28] [29]

$$\Lambda_g \approx \frac{\Lambda_s \Lambda_r}{\mu_0/g} \qquad (3)$$

where g is air-gap length, respectively. Λ_s and Λ_r are the air-gap permeance functions by taking the stator and rotor slotting effects into account, respectively. When initial rotor position is in the axis of phase A windings, Λ_s and Λ_r can be described by

$$\Lambda_s = \Lambda_{s0} + \sum_{m=1} \Lambda_{sm} \cos(mZ_s\theta) \qquad (4)$$

$$\Lambda_r = \Lambda_{r0} + \sum_{n=1} \Lambda_{rn} \cos\left[nZ_r(\theta - \Omega_r t)\right] \qquad (5)$$

where Λ_{s0} and Λ_{r0} are the 0th stator and rotor permeance coefficients, respectively. Λ_{sm} and Λ_{rn} are the mth and n^{th} stator and rotor permenace coefficients, respectively. Thus, the synthesized air-gap permeance function can be further rewritten as

$$\Lambda_g = \frac{g}{2\mu_0} \sum_{m=0}^{\infty} \sum_{n=0}^{\infty} \Lambda_{sm} \Lambda_{rn} \cos\left[(mZ_s \pm nZ_r)\theta \mp nZ_r\Omega_r t\right] \quad (6)$$

By using PM MMF-permeance based method [30], the no-load air-gap flux density can be obtained as

$$B_g = \left(F_{SPM} + F_{RPM}\right)\Lambda_g = B_{g\_SPM} + B_{g\_RPM} \qquad (7)$$

where B_{g_SPM} and B_{g_RPM} are the no-load air-gap flux densities due to stator and rotor PMs, respectively. The B_{g_SPM} can be further rewritten as

$$B_{g\_SPM} = \frac{g}{4\mu_0} \sum_{i=0}^{\infty} \sum_{m=0}^{\infty} \sum_{n=0}^{\infty} F_{SPMi} \Lambda_{sm} \Lambda_{rn} \times$$
$$\sin\left[(nZ_r \pm mZ_s \pm iZ_s)\theta - nZ_r\Omega_r t\right] \qquad (8)$$

Similarly, B_{g_RPM} can be further rewritten as

$$B_{g\_RPM} = \frac{g}{4\mu_0} \sum_{j=0}^{\infty} \sum_{m=0}^{\infty} \sum_{n=0}^{\infty} F_{RPMj} \Lambda_{sm} \Lambda_{rn} \times$$
$$\sin\left[(nZ_r \pm mZ_s \pm jZ_r)\theta - (n \pm j)Z_r\Omega_r t \mp jZ_r\theta_0\right] \qquad (9)$$

Considering the fluxes passing through phase A, the flux linkage of phase A can be given as

$$\psi_A(t) = r_g l_{stk} \int_0^{2\pi} B_g N_a(\theta) d\theta \qquad (10)$$

where l_{stk} is the active stack length, r_g is the air-gap radius. $N_a(\theta)$ is the winding function, which can be expressed as [31]

$$N_a(\theta) = \sum_{h=1} \frac{2}{h\pi} N_s k_{wh} \cos(h\theta) \qquad (11)$$

where N_s is the number of series-connected turns per phase, k_{wh} is the winding factor of the hth air-gap flux density. Consequently, the back-EMF of phase A can be obtained by

$$e_a(t) = -\frac{d\psi_A(t)}{dt} = e_{SPM} + e_{RPM} \qquad (13)$$

The electromagnetic torque of DSPM machines can also be derived as

$$T_e = (e_A i_A + e_B i_B + e_C i_C)/\Omega_r \qquad (14)$$

where e_A, e_B and e_C are the back-EMFs of phases A, B and C, respectively. i_A, i_B and i_C are the currents of phases A, B and C, respectively. When neglecting the reluctance torque, the average torque can be further expressed as

$$T_{avg} = \frac{3}{2} \frac{I_A E_A}{\Omega_r} = T_{SPM} + T_{RPM} \qquad (15)$$

where I_A is the phase current. E_A is the phase back-EMF amplitude. T_{SPM} and T_{RPM} are the average torque components due to stator and rotor PMs, respectively. Taking the main-order air-gap field working harmonics into consideration, the average torques due to the stator and rotor PMs can be further rewritten as

$$T_{SPM} = 3r_g l_{stk} N_s I_A Z_r \times$$

$$\left\{ \begin{array}{l} B_{|2Z_s-Z_r|}\frac{k_{w|2Z_s-Z_r|}}{P_{|2Z_s-Z_r|}} + B_{|3Z_s-Z_r|}\frac{k_{w|3Z_s-Z_r|}}{P_{|3Z_s-Z_r|}} + B_{|Z_s-Z_r|}\frac{k_{w|Z_s-Z_r|}}{P_{|Z_s-Z_r|}} + \\ B_{|3Z_s-2Z_r|}\frac{k_{w|3Z_s-2Z_r|}}{P_{|3Z_s-2Z_r|}} + B_{|Z_s+Z_r|}\frac{k_{w|Z_s+Z_r|}}{P_{|Z_s+Z_r|}} + B_{|2Z_s+Z_r|}\frac{k_{w|2Z_s+Z_r|}}{P_{|2Z_s+Z_r|}} + \\ B_{|2Z_s-2Z_r|}\frac{k_{w|2Z_s-2Z_r|}}{P_{|2Z_s-2Z_r|}} + B_{|3Z_s+Z_r|}\frac{k_{w|3Z_s+Z_r|}}{P_{|3Z_s+Z_r|}} \end{array} \right\} \qquad (16)$$

$$T_{RPM} = 3r_g l_{stk} N_s I_A Z_r \times$$

$$\left\{ \begin{array}{l} B_{|2Z_s-Z_r|}\frac{k_{w|2Z_s-Z_r|}}{P_{|2Z_s-Z_r|}} + B_{|3Z_s-Z_r|}\frac{k_{w|3Z_s-Z_r|}}{P_{|3Z_s-Z_r|}} + B_{|Z_s-Z_r|}\frac{k_{w|Z_s-Z_r|}}{P_{|Z_s-Z_r|}} + \\ B_{|Z_r|}\frac{k_{w|Z_r|}}{P_{|Z_r|}} + B_{|2Z_s-2Z_r|}\frac{k_{w|2Z_s-2Z_r|}}{P_{|2Z_s-2Z_r|}} + B_{|Z_s+Z_r|}\frac{k_{w|Z_s+Z_r|}}{P_{|Z_s+Z_r|}} + \\ B_{|2Z_s+Z_r|}\frac{k_{w|2Z_s+Z_r|}}{P_{|2Z_s+Z_r|}} + B_{|2Z_r|}\frac{k_{w|2Z_r|}}{P_{|2Z_r|}} + B_{|3Z_s+Z_r|}\frac{k_{w|3Z_s+Z_r|}}{P_{|3Z_s+Z_r|}} \end{array} \right\} \qquad (17)$$

where I_A is the peak value of phase current. The average torque can be expressed as a unified form

$$T_{avg} = 3r_g l_{stk} N_s I_A \sum_j \frac{Z_r}{P_j} B_i k_{wj} = \sum_{j=1} T_{avgj} \qquad (18)$$

where B_j, k_{wj} and P_j are the amplitude, winding factor and pole pairs of the jth air-gap flux density. T_{avgj} is the average torque generated by the jth air-gap flux density.

B. MMF Modelling Torque Quantification by a Hybrid FE/Analysis Method

In order to quantify the torque contributions of the multiple working harmonics, a hybrid FE/analytical method is proposed, the flowchart of which is shown in Fig. 2. The no-load air-gap flux density distribution can be obtained by static magnetic field simulation, which requires significantly reduced computation time compared with transient simulation. Besides, the open-circuit air-gap flux densities due to stator and rotor PMs can be separated by the well-known frozen permeability method. Then, the torque contributions of the main-order working harmonics can be quantified by a unified average torque equation. In addition, the torque proportion due to the jth air-gap flux density can be determined by

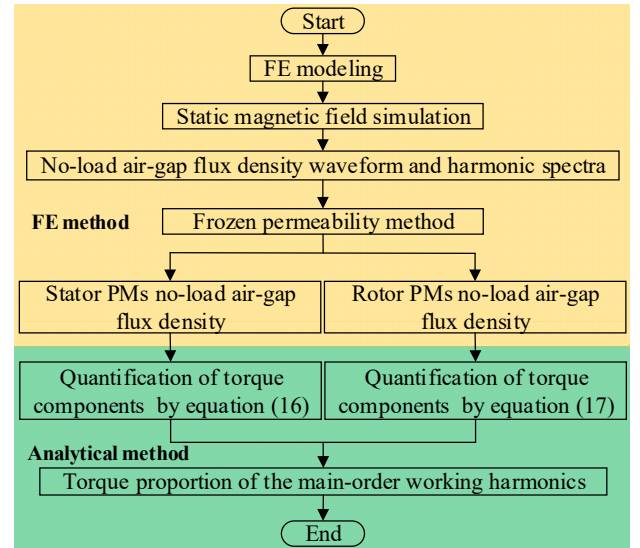$$\lambda_j = \frac{T_{avgj}}{T_{avg}} \times 100\% \qquad (19)$$

Fig. 2. The flowchart of the proposed hybrid FE/analytical method.

In order to confirm above-mentioned analysis, the torque characteristics are illustrated in Fig. 3. The average torques due to stator and rotor PMs can be separated by employing frozen permeability method [32], as shown in Fig. 3(a). The corresponding individual and total torque waveforms are illustrated in Fig. 3(b). The torque proportions due to various harmonics can be obtained by (23), as shown in Fig. 3(c). The detailed torque contributions of the working harmonics are tabulated in Table II. It can be seen that various harmonics are involved in the torque production in DSPM machine. Besides, because of the pronounced biased field modulation effect, the low-order harmonics, i.e., $|2Z_s-Z_r|$ (2nd) and $|3Z_s-Z_r|$ (4th), contribute the relatively higher torque proportion than other components. Moreover, the torque proportion of various harmonics due to the stator and rotor PMs are illustrated in Fig. 3(d). It can be observed that the $|2Z_s-Z_r|$ (2nd) and Z_r (14th) order harmonics contribute the relatively higher torque proportions in rotor PMs excitation, while the $|2Z_s-Z_r|$ (2nd) and $|3Z_s-Z_r|$ (4th) order harmonics exhibit higher torque proportion in stator PMs excitation, which is mainly due to the fact that the BFME results

in relatively higher harmonic amplitudes. The torque contributions of the main working harmonics are tabulated in Table II. It can be observed from the analytical predictions that the stator and rotor PMs contribute 54.73% and 45.27% to the total average torque, respectively, which are in good agreement with those 2D FE predicted values. Besides, because only the main working harmonics are taken into consideration in the analytical model, the analytically predicted total torques due to stator and rotor PMs are slightly lower than the 2D FE predicted ones.
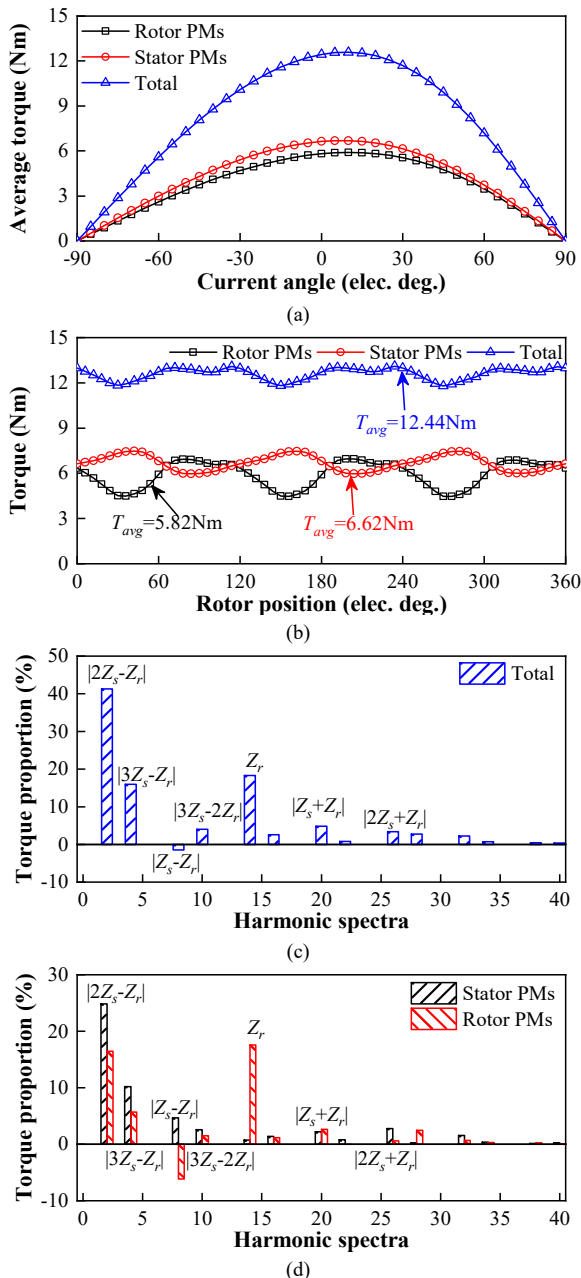
Fig. 3. Torque characteristics. (a) Average torque versus current angle curves. (b) Stead-state torques. (c) Torque proportion due to main working harmonics. (d) Torque proportion due to main working harmonics of the stator and rotor PMs.

TABLE II
TORQUE CONTRIBUTIONS DUE TO VARIOUS WORKING HARMONICS IN DSPM MACHINE

Items	DSPM machine		
	T_{SPM}	T_{RPM}	Total
	B (T) / T_{avg}(Nm) / λ(%)	B (T) / T_{avg} (N m) / λ(%)	λ (%)
$|2Z_s{-}Z_r|$ (2th)	0.133 / 3.079 / **25.467**	0.088 / 2.037 / **16.849**	**42.306**
$|3Z_s{-}Z_r|$ (4th)	0.109 / 1.273 / **10.529**	0.061 / 0.710 / **5.873**	**16.402**
$|Z_s{-}Z_r|$ (8th)	0.100 / 0.579 / 4.789	0.131/ -0.758 / -6.270	-1.481
$|3Z_s{-}2Z_r|$ (10th)	0.068 / 0.318 / 2.630	0.039 / 0.185 / 1.483	4.040
Z_r (14th)	0.028 / 0.094 / 0.755	0.661 / 2.168 / **17.932**	**18.687**
$|2Z_s{-}2Z_r|$ (16th)	0.059 / 0.171 / 1.414	0.050 / 0.146 / 1.175	2.589
$|Z_s{+}Z_r|$ (20th)	0.119 / 0.276 / 2.282	0.142 / 0.329 / 2.721	5.003
$|2Z_s{+}Z_r|$ (26th)	0.195 / 0.347 / 2.787	0.041 / 0.073 / 0.604	1.391
$|2Z_r|$ (28th)	0.020 / 0.034 / 0.281	0.185 / 0.307 / 2.539	2.820
$|3Z_s{+}Z_r|$ (32th)	0.134 / 0.195 / 1.569	0.062 / 0.089 / 0.723	2.292
$|Z_s{+}2Z_r|$ (34th)	0.034 / 0.047 / 0.376	0.031 / 0.042 / 0.339	0.714
$|4Z_s{+}Z_r|$ (38th)	0.017 / 0.021 / 0.165	0.029 / 0.036 / 0.287	0.452
$|2Z_s{+}2Z_r|$ (40th)	0.031 / 0.035 / 0.285	0.009 / 0.010 / 0.081	0.366
$|5Z_s{+}Z_r|$ (44th)	0.038 / 0.039/ 0.319	0.045 / 0.047 / 0.380	0.699
$|3Z_s{+}2Z_r|$ (46th)	0.018 / 0.018 /0.021	0.020 / 0.021 / 0.165	0.312
$|6Z_s{+}Z_r|$ (50th)	0.017 / 0.016 /0.128	0.003 / 0.003 / 0.023	0.151
Sum T_{avg} (Nm)/λ(%)	**6.617 / 54.73%**	**5.473 / 45.27%**	**12.090**
FE T_{avg} (Nm)/λ(%)	**6.62 /53.22%**	**5.82 / 46.78%**	**12.44**

IV. PERFORMANCE COMPARISON OF THE PROPOSED AND CONVENTIONAL DSPM MACHINES

A. Torque Capability

In order confirm the merits of the proposed machine, a conventional DSPM machine with stator consequent-pole PM design, as shown in Fig. 4, is selected to present a performance comparison. The detailed design parameters are listed in Table III. In order to perform a fair comparison, the three machines share the same stator outer diameter, stack length, PM volume and current density, as illustrated in Table V. Besides, compared with proposed DSPM machine with U-shaped PM structure, the existing DSPM configuration exhibits relatively larger flux leakage and hence resulting in more magnetic saturation in stator and rotor teeth, as illustrated in Fig. 4, which indicates that the existing DSPM machine exhibits a higher iron loss, a lower PM utilization and torque capability. The torque characteristics of the three machines are shown in Fig. 5. Due to the flux concentrated effect and hence improved working harmonics, the proposed stator U-shaped DSPM machine exhibits 40.41% higher torque density than the existing DSPM structure. In addition, it can be seen that the proposed DSPM machine exhibits the highest torque/PM volume ratio at rated-load, as shown in Table III, which indicates the best cost-effectiveness can be obtained by employing the U-shaped PM design.
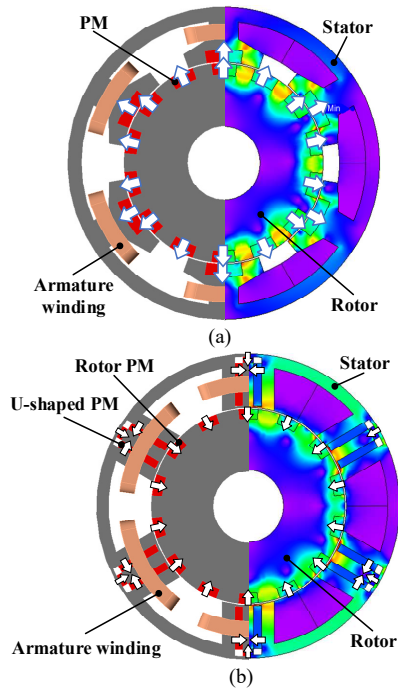
(a)

(b)

Fig. 4. Machine topologies and their no-load flux density distributions. (a) Existing DSPM machine with stator consequent-pole PM design. (b) Proposed DSPM machine.

TABLE III
MAIN DESIGN PARAMETERS OF THE EXISTING AND PROPOSED DSPM MACHINES

Items	Existing DSPM	Proposed DSPM
Number of stator slots	6	
Number of rotor PM pole pairs	14	
Stator outer diameter, mm	102	
Stack length, mm	50	
Air-gap length, mm	0.5	
Stator inner diameter, mm	66.2	
Steel grade	35CS250	
PM grade	N42SH	
PM volume, cm^3	41.63	
Rated current, A	8	
Average torque, Nm	8.86	12.44
Torque/PM volume, Nm/L	212.8	298.8

(a)

(b)

(c)
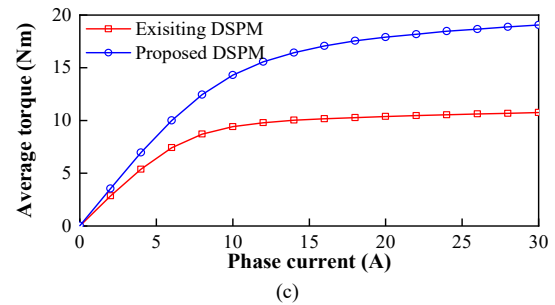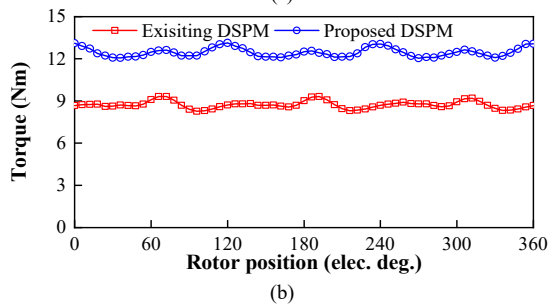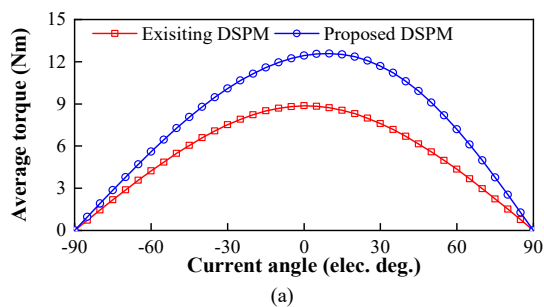
Fig. 5. Comparison of the torque characteristics of the proposed and existing DSPM machines. (a) Average torque versus current angle. (b) Steady-state torque. (c) Average torque versus phase current.

B. Loss and Efficiency

The loss characteristics of the two DSPM machines with different rotor speeds are illustrated in Fig. 6. Because of the serious flux leakage, the existing DSPM structure exhibits higher iron loss than the proposed DSPM machine regardless of rotor speed, as shown in Fig. 6(a). Due to the flux concentrated effect, the proposed DSPM machine shows higher lower-order working harmonics. Besides, the U-shaped PM design provides a magnetic circuit for lower-order air-gap flux density harmonics and hence resulting in a relatively lower reluctance for armature-reaction flux and higher PM eddy-current density in proposed DSPM machine. As a result, the proposed DSPM design presents a relatively higher PM eddy-current loss than the existing DSPM machine regardless of rotor speed, as shown in Fig. 6(b). The efficiency maps of the two DSPM machines are shown in Fig. 7. Because of the significantly reduced iron loss and relatively higher torque capability, the proposed DSPM machine exhibits higher high-efficiency (over 90%) region than conventional DSPM machine, which confirms the merit of the proposed design in terms of the efficiency improvement.
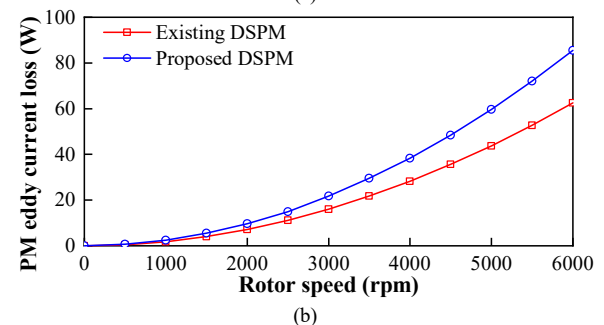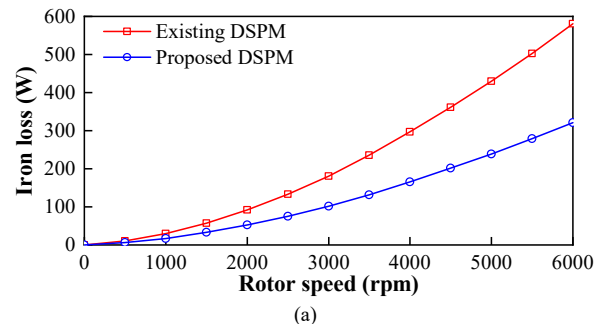

(a)

(b)

Fig. 6. Iron and PM eddy-current losses. (a) Iron loss. (b) PM eddy-current loss.
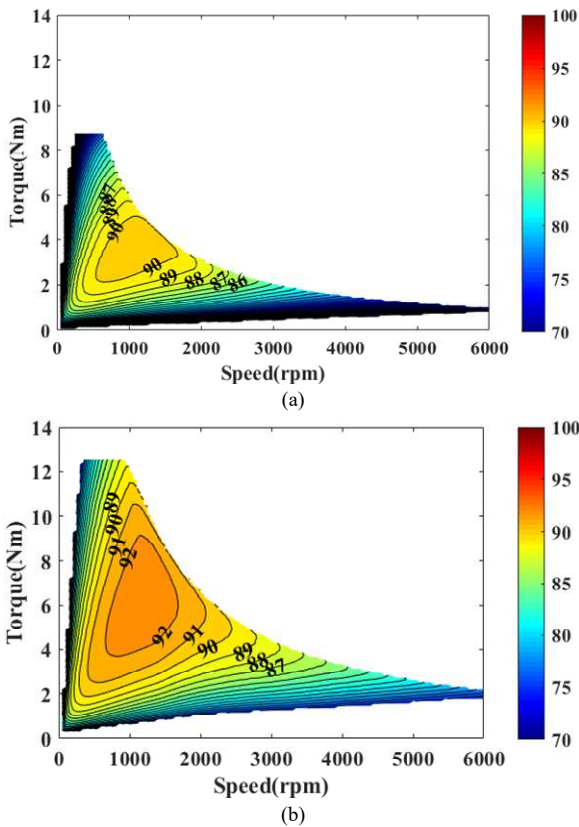
(a)

(b)

Fig. 7. Efficiency maps of the DSPM machines. (a) Existing DSPM machine. (b) Proposed DSPM machine. (I_{rms}=8 A, U_{dc}=120 V)

V. PROTOTYPING AND EXPERIMENTAL VALIDATION

A. Parallel Complementary Design for Cogging Torque Reduction

In order to reduce the cogging torque and torque ripple, the PC design is adopted [33], as shown in Fig. 8. It can be observed that the two parts rotor shift β_{PM}=π/Z_r mechanical degree. In addition, the PMs in stator and rotor sides share the same polarity in rear and front parts. The back-EMF waveforms and their harmonic spectra of the DSPM machine with PC (w/ PC) and without PC (w/o PC) designs are illustrated in Fig. 9. It can be seen that the two-part rotors have N and S pole PMs, the corresponding coil and hence phase back-EMFs exhibit a phase difference with a π electrical degree. Thus, in order to gain the same initial phase angle of the back-EMFs, the two-part rotors are shifted with a π/Zr mechanical degree. Besides, due to the PC design, the even-order harmonics of back-EMF can be significantly reduced, as shown in Fig. 9(b), which indicates that the torque ripple can be effectively reduced in PC design. In addition, it should be noted that the fundamental component of PC design is approximate to that of the original model. The cogging torque waveforms and harmonic spectra of the DSPM machines without and with PC designs are illustrated in Fig. 10. It can be found that the peak values can be effectively reduced 59.7% by adopting PC design, which is mainly due to the canceled 3rd harmonic and effectively reduced 6th harmonic in proposed PC design, as shown in Fig. 10(b).
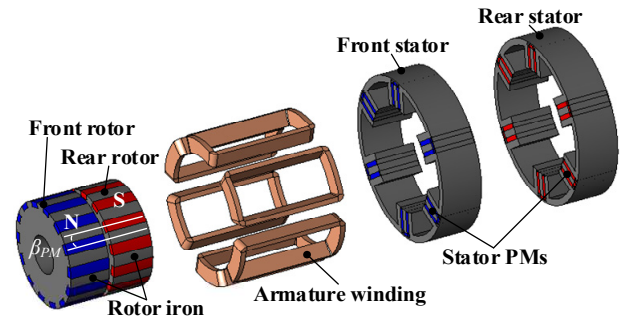

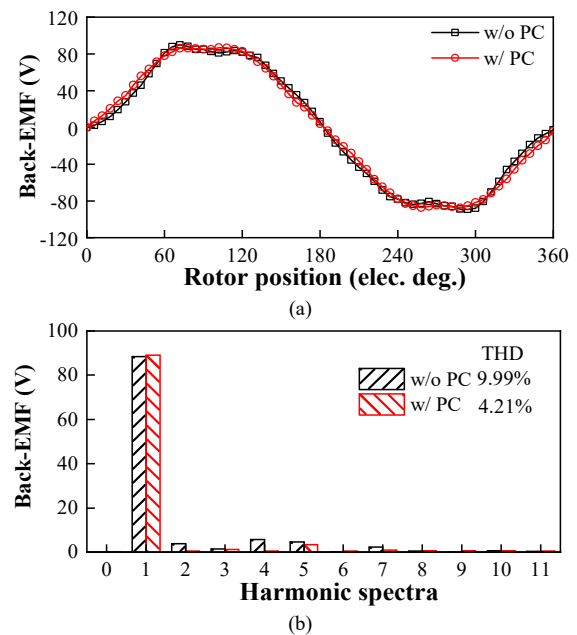Fig. 8. Machine topology of the DSPM machine with PC design.

(a)

(b)

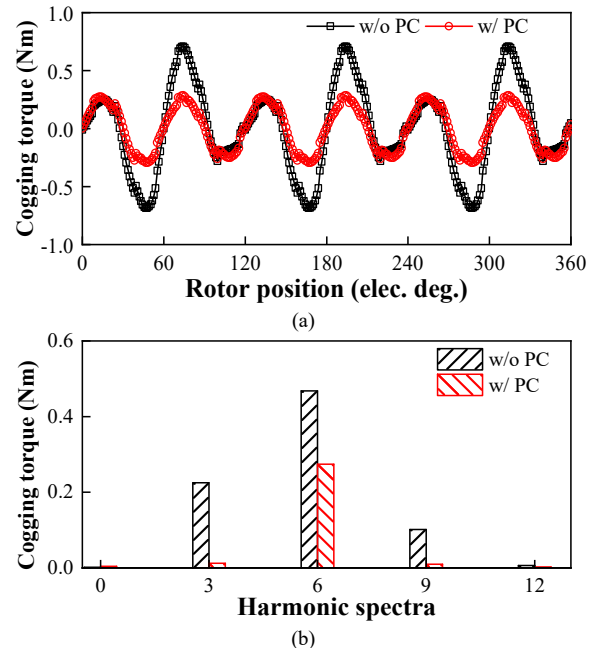Fig. 9. Back-EMFs @ 1000 r/min. (a) Waveforms. (b) Harmonic spectra.

(a)

(b)

Fig. 10. Comparison of the cogging torque without and with PC design. (a) Waveforms. (b) Harmonic spectra.

B. Final Prototype, Test Rig, and Experimental Results

In order to experimentally validate abovementioned analyses, a 6-slot/14-pole-pair DSPM machine with PC design is manufactured and tested. The stator and rotor assemblies are shown in Fig. 11. The test-rig of cogging torque experiment is illustrated in Fig. 12. The balanced beam was attached to the prototype rotor shaft. When the dividing dial drives the prototype with a rotate angle, a value can be obtained on electronic scale [34]. The measured and 3D FE predicted cogging torque waveforms and their harmonic spectra are shown in Fig. 13. It can be seen that the measured cogging torque values are slightly higher than 3D FE predicted, which is mainly due to mechanical tolerance. In addition, the comparison of the measured and 3D FE predicted back-EMF and torque results are given in Figs. 14 and 15, respectively. Similarly, due to manufactured mechanical tolerance in prototype, the measured back-EMF and average torque values are slightly lower than 3D FE predicted. Because of the mechanical tolerance and slightly increased mechanical loss in high speed region, the difference between them is slightly increased with speed. Overall, the satisfactory agreement between the measured and 3D FE results confirm the effectiveness of the above analyses.
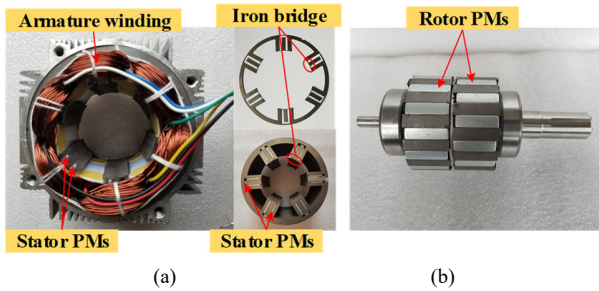

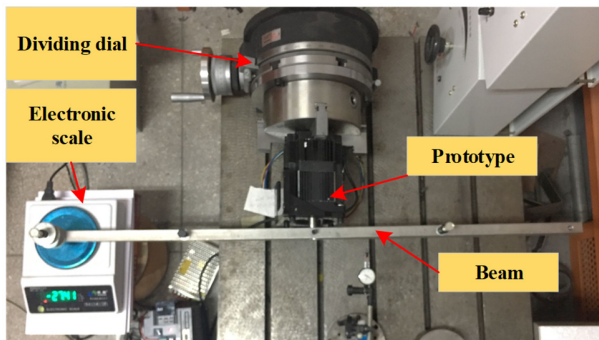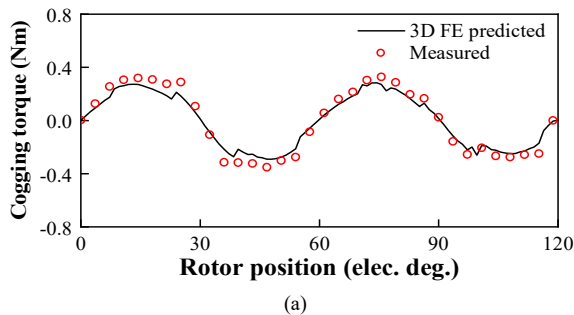Fig. 11. The prototype of proposed DSPM machine. (a) Stator core and armature windings. (b) PC rotor.

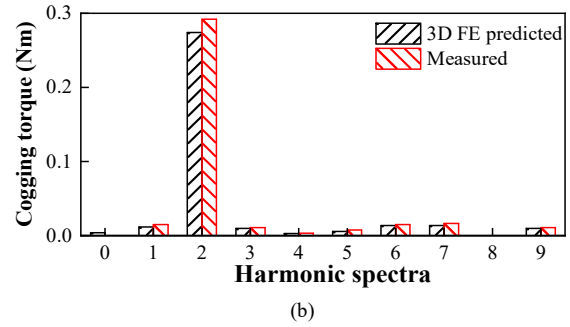Fig. 12. The test-rig of cogging torque experiment.

(a)

(b)

Fig. 13. Comparison of 3D FE-predicted and measured cogging torque. (a) Waveforms. (b) Harmonic spectra.
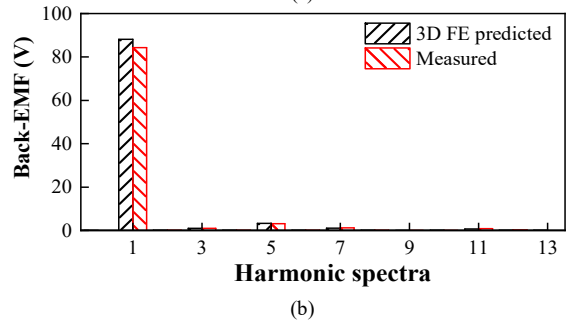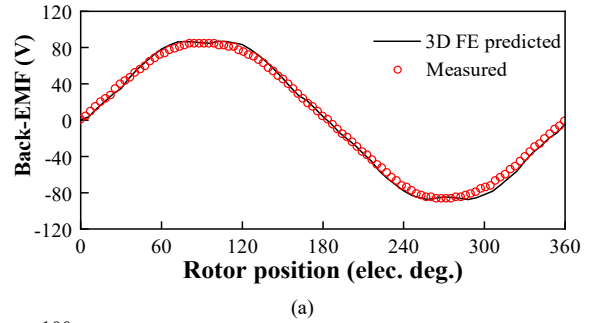

(a)

(b)

Fig. 14. Comparison of measured and 3D FE-predicted back-EMFs. (a) Waveforms. (b) Harmonic spectra.

T_{avg}=11.35Nm, T_{rip}=6.34%

T_{avg}=10.85Nm, T_{rip}=9.79%

(a)

(b)
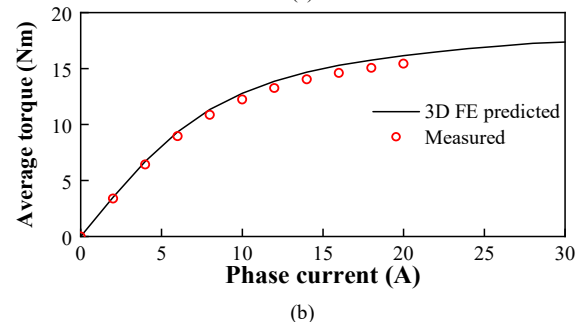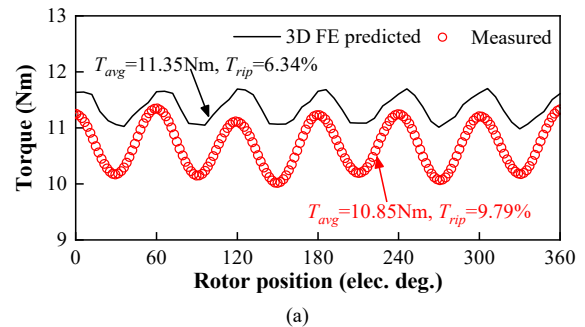
Fig. 15. Comparison of 3D FE-predicted and measured torque. (a) Stead-state torque waveforms (i_q=10A, i_d=0A). (b) Average torque versus phase current.

VI. Conclusions

This paper proposes a new DSPM machine with stator U-shaped PMs and rotor consequent pole magnets. A simple hybrid FE/analytical method is adopted to identify and quantify the torque contributions of the various effective air-gap field harmonics by employing a unified torque equation. It can be found that the low-order harmonics, i.e., $|2Z_s\text{-}Z_r|$ (2nd) and $|3Z_s\text{-}Z_r|$ (4th), contribute relatively higher torque proportion than the other components. Besides, in terms of the rotor PM excitation, the $|2Z_s\text{-}Z_r|$ (2nd) and Z_r (14th) order harmonics are mainly responsible for the torque generation. While for the stator PM side, the $|2Z_s\text{-}Z_r|$ (2nd) and $|3Z_s\text{-}Z_r|$ (4th) order harmonics show higher torque proportions, which are mainly due to the fact that the BFME results in relatively higher harmonic amplitudes. Compared with the conventional DSPM machines with stator consequent-pole PM design, the proposed machine exhibits higher torque capability and larger high-efficiency (over 90%) region, which confirms the effectiveness of torque and efficiency improvement by employing the U-shaped PM structure. Besides, a PC design is employed, which can reduce the cogging torque 59.7% due its even-order harmonics cancellation effect. Finally, the DSPM machine with PC design is manufactured and tested, and the satisfactory agreement between experimental and FE predicted results validates the theoretical and FE analyses.

Acknowledgment

References

[1] V. Madonna, P. Giangrande, W. Zhao, H. Zhang, C. Gerada, and M. Galea, "Electrical Machines for the More Electric Aircraft: Partial Discharges Investigation," *IEEE Trans. Ind. Appl.*, vol. 57, no. 2, pp. 1389–1398, Mar. 2021.

[2] S. Nategh, A. Boglietti, Y. Liu, D. Barber, R. Brammer, D. Lindberg and O. Aglen, "A Review on Different Aspects of Traction Motor Design for Railway Applications," *IEEE Trans. Ind. Appl.*, vol. 56, no. 3, pp. 2148–2157, May 2020.

[3] A. M. El-Refaie, "Toward a sustainable more electrified future: the role of electrical machines and drives," *IEEE Electrifi. Maga.*, vol. 7, no. 1, pp. 49-59, Mar. 2019.

[4] M. Cheng, W. Hua, J. Zhang and W. Zhao, "Overview of stator-permanent magnet brushless machines," *IEEE Trans. Ind. Electron.*, vol. 58, no. 11, pp. 5087-5101, Nov. 2011.

[5] A. Ishizaki, T. Tanaka, K. Takasaki and S. Nishikata, "Theory and optimum design of PM Vernier motor," in *Proc. 1995 Seventh Int. Conf. Elec. Mach. & Drives*, 1995, pp. 218-212.

[6] Q. Wang and S. Niu, "A novel hybrid-excited dual-PM machine with bidirectional flux modulation," *IEEE Trans. Energy Convers*, vol. 32, no. 2, pp. 424-435, Jun. 2017.

[7] L. Xu. W. Zhao, M. Wu and J. Ji, "Investigation of slot-pole combination of dual-permanent-magnet-excited vernier machines by using air-gap field modulation theory," *IEEE Trans. Transport. Electrific.*, vol. 5, no. 4, pp. 1360-1369, Dec. 2019.

[8] X. Zhao, S. Niu and W. Fu, "Design of a novel parallel-hybrid-excited dual-PM machine based on armature harmonics diversity for electric vehicle propulsion," *IEEE Trans. Ind. Electron.*, vol. 66, no. 6, pp. 4209-4219, Jun. 2019.

[9] X. Zhao, S. Niu, X. Zhang and W. Fu, "A new relieving-DC-saturation hybrid excitation vernier machine for HEV starter generator application," *IEEE Trans. Ind. Electron.*, vol. 67, no. 8, pp. 6342-6353, Aug. 2020.

[10] H. Fan, K. T. Chau, L. Cao and C. Jiang, "Design and analysis of a new bipolar-flux DSPM linear machine," *IEEE Trans. Energy Convers.*, vol. 33, no. 4, pp. 2081-2090, Dec. 2018.

[11] S. Shimomura, M. Fujieda and K. Hoshino, "Studies to decrease cogging force and pulsating thrust in the prototype linear permanent magnet vernier motor," in *Proc. 2008 Int. Conf. Elec. Mach & Sys. (ICEMS)*, 2008, pp. 3417-3422.

[12] H. Wang and S. Fang, "Design of new dual-stator field modulation machines," *IEEE Trans. Ind. Electron.*, vol. 67, no. 7, pp. 5626-5636, Jul. 2020.

[13] R. Ishikawa, K. Sato, S. Shimomura and R. Nishimura, "Design of in-wheel permanent magnet vernier machine to reduce the armature current density," in *Proc. 2013 Int. Conf. Elec. Mach & Sys (ICEMS)*, 2013, pp. 459-464.

[14] S. Niu, S. L. Ho and W. N. Fu, "A novel stator and rotor dual PM vernier motor with space vector plus width modulation," *IEEE Trans. Magn.*, vol. 50, no. 2, Feb. 2014, Art. no. 7019904.

[15] Y. Yamada and K. Akatsu, "A new motor with stator magnet using the magnetization reversal technique," in *Proc. 2016 Int. Conf. Elec. Mach. (ICEM)*, 2016, pp. 60-65.

[16] Q. Wang and S. Niu, "Electromagnetic design and analysis of a novel fault-tolerant flux-modulated memory machine," *Energies*, vol. 8, pp. 8069-8085, 2015.

[17] Q. Wang, S. Niu and L. Yang, "Design optimization and comparative study of novel dual-PM excited machines," *IEEE Trans. Ind. Electron.*, vol. 64, no. 12, pp. 9924-9933, Nov. 2017.

[18] Y. Shi and L. Jian, "A novel dual-permanent-magnet-excited machine with flux strengthening effect for low-speed large-torque applications," *Energies*, vol. 11, no. 153, pp.1-17, 2018.

[19] Y. Kataoka, M. Takayama, Y. Matsushima and Y. Anazawa, "Design of high torque PM vernier motor," in *Proc. 2016 Int. Conf. Elec. Mach. & Sys. (ICEMS)*, 2016, pp. 1-6.

[20] Y. Kataoka, Y. Matsushima and Y. Anazawa, "A design for PM vernier motors," in *Proc. 2018 Int. Conf. Elec. Mach. & Sys. (ICEMS)*, 2018, pp. 87-92.

[21] L. Jian, Y. Shi, C. Liu, G. Xu, Y. Gong and C. C. Chan, "A novel dual-permanent-magnet-excited machine for low-speed large-torque applications," *IEEE Trans. Magn.*, vol. 49, no. 5, pp. 2381-2383, Nov. 2013.

[22] L. Jian, Y. Shi, J. Wei, Y. Zheng and Z. Deng, "Design optimization and analysis of a dual-permanent-magnet-excited machine using response surface methodology," *Energies*, no. 8, pp. 10127-10140, 2015.

[23] Y. Gao, M. Doppelbauer, R. Qu, D. Li and H. Ding, "Synthesis of a flux modulation machine with permanent magnets on both stator and rotor," *IEEE Trans. Ind. Appl.*, vol. 57, no. 1, pp, 294-305, Jan. /Feb. 2021.

[24] L. Xu, W. Zhao, G. Liu, J. Ji and S. Niu, "A novel dual-permanent-magnet-excited machine with non-uniformly distributed permanent-magnets and flux modulation poles on the stator," *IEEE Trans. Vehi. Tech.*, vol. 69, no. 7, pp. 7104-7115, Jul. 2020.

[25] Y. Li, H. Yang and H. Lin, "Analysis of dual-sided permanent magnet machines with complementary stator structures," in *Proc. 2019 Int. Conf. Elec. Mach. & Sys. (ICEMS)*, 2019, pp. 1-6.

[26] Y. Li, H. Yang, H. Lin, W. Liu and S, Lyu, "A novel dual-sided PM machine with stator spoke-type PM structure," in *Proc. 2019 IEEE Energy Conver. Congre. Expo. (ECCE)*, 2019, pp. 1721-1728.

[27] H. Yang, Y. Li, H. Lin, W. Liu and X. Zhao, "Novel dual-sided permanent magnet machines with different stator magnet arrangements," in *Proc. 2019 IEEE Energy Conver. Congre. Expo. (ECCE)*, 2019, pp. 6114-6121.

[28] B. Heller and V. Hamata, *Harmonic Field Effects in Induction Machines*. Amsterdam, The Netherlands: Elsevier, 1977.

[29] D. Li, R. Qu, J. Li, W. Xu, and L. Wu, "Synthesis of Flux Switching Permanent Magnet Machines," *IEEE Trans. Energy Convers.*, vol. 31, no. 1, pp. 106–117, Mar. 2016

[30] A. Toba and T. A. Lipo, "Generic torque-maximizing design methodology of surface permanent-magnet vernier machine," *IEEE Trans. Ind. Appl.*, vol. 36, no. 6, pp. 1539-1546, Nov. /Dec. 2000.

[31] T. A. Lipo, *Introduction to AC Machine Design*, 3rd ed. Madison, WI: Wisconsin Power Electronics Research Center, 2016.

[32] W. Q. Chu and Z. Q. Zhu, "Average torque separation in permanent magnet synchronous machines using frozen permeability," *IEEE Trans. Magn.*, vol. 49, no. 3, pp. 1202-1210, Mar. 2013.

[33] J. Li, K. Wang and F. Li, "Reduction of torque ripple in consequent-pole permanent magnet machines using staggered rotor," *IEEE Trans. Energy Convers.*, vol. 34, no. 2, pp. 643-651, Jun. 2019.

[34] Z. Q. Zhu, "A simple method for measuring cogging torque in permanent magnet machines," in *Proc. 2009 IEEE Power & Energy Soc. Gen. Meeting*, 2009, pp. 1-4.